

On the stability of gravity-driven liquid films overflowing microstructures with sharp corners

Henning Bonart,^{*} Johannes Jung, and Jens-Uwe Repke[†]
*Technische Universität Berlin, Process Dynamics and Operations Group,
Strae des 17. Juni 135, 10623 Berlin, Germany*

(Dated: February 12, 2020)

We are concerned with the stability of thin liquid films overflowing single microstructures with sharp corners. The microstructures were of rectangular and triangular shape. Their heights and widths were 0.25, 0.5 and 0.75 times the Nusselt film thickness. To observe smooth, wavy and very unstable films we performed simulations with Reynolds numbers ranging from 10 to 70. The dynamics of the liquid film and the overflowing gas phase were described by the coupling between the Cahn–Hilliard and Navier–Stokes equations. The resulting model forms a very tightly coupled and nonlinear system of equations. Therefore we carefully selected the solution strategy to enable efficient and accurate large-scale simulations. Our results showed that the formation of waves was shifted to higher Reynolds numbers compared to the film on a smooth surface. If waves were finally formed the microstructures led to irregular waves. Our results indicate a great influence of the microstructure’s shape and dimension on the stability of the overflowing liquid film.

arXiv:2002.04293v1 [physics.flu-dyn] 11 Feb 2020

^{*} henning.bonart@tu-berlin.de

[†] jens-uwe.repke@tu-berlin.de; www.dbta.tu-berlin.de

I. INTRODUCTION

Gravity-driven liquid films overflowing a solid, structured surface appear in numerous technical applications. Examples include falling film evaporators or structured high performance packing for absorption columns. For research conducted on the stability of thin liquid films flowing on smooth and flat substrates and the formation of waves we refer to the recent review by Aksel and Schörner [1, Ch.5]. In the literature, some results were documented on the influence of smooth microstructures, like hemispheres ([2, 3]), on the stability of liquid films, see the review by Craster and Matar [4, Ch. VII. A]. It is well-known for single phase flows, that sharp corners have a great influence on stability and flow separation, see for example [5–8]. Surprisingly, to the best of our knowledge only few papers discuss results on thin liquid films and single microstructures with sharp corners and positive elevation in the size of the film itself. Almost sharp structures like rectangles with rounded corners were simulated by [9]. Results on trenches or single step-ups or -downs with sharp corners were described by [3, 10, 11]. However, despite their relevance in technical applications, systematic studies of the influence of single, sharp microstructures on the stability of the film are rarely found.

In this paper we report on detailed numerical simulations of films overflowing single microstructures with sharp corners. The dynamics of the two-phase flow are described by the coupling between the Cahn–Hilliard (CH) and the Navier–Stokes (NS) equations. In this way, we are able to fully resolve the sharp corners. The resulting model forms a very tightly coupled and nonlinear system of equations. Therefore we carefully select the solution strategy to enable efficient and accurate simulations. This includes the linearization and decoupling of the equations and preconditioned Krylov methods for the solution of the arising linear systems. The examined microstructures are of rectangular and triangular shape with heights and widths of 0.25, 0.5 and 0.75 compared to the particular Nusselt film thickness. The Reynolds numbers range from 10 to 70.

The remainder of the article is structured as follows: In Section II, we discuss the governing equations and present the system in nondimensional form. The numerical method is described in Section III. Here, we give details on the decoupling of the equations, the discretization and the preconditioner. The test case is described in Section IV. Finally, we present and discuss our results in Section V. In Section VI we conclude our paper.

II. CAHN–HILLIARD–NAVIER–STOKES EQUATIONS

We treated the liquid film as well as the overflowing gas phase as Newtonian, isotherm, immiscible and incompressible fluids. The thermodynamically consistent Cahn–Hilliard–Navier–Stokes model presented in [12] was applied. The model combines the common incompressible, single-field Navier–Stokes (NS) equations with the convective Cahn–Hilliard (CH) equations to describe the interface dynamics between the liquid and the gas. It is given by:

$$\rho \partial_t v + ((\rho v + J) \cdot \nabla) v - \operatorname{div}(2\eta Dv) + \nabla p = -\varphi \nabla \mu + \rho g, \quad (1)$$

$$-\operatorname{div}(v) = 0, \quad (2)$$

$$\partial_t \varphi + v \cdot \nabla \varphi - b \Delta \mu = 0, \quad (3)$$

$$-\sigma \epsilon \Delta \varphi + \frac{\sigma}{\epsilon} W'(\varphi) = \mu, \quad (4)$$

with the velocity field v , the pressure field p , the phase field φ and the chemical potential μ . The velocity deformation tensor and the gravitational acceleration are given by $2Dv := \nabla v + (\nabla v)^t$ and g . The density function is denoted by $\rho(\varphi)$ and satisfies $\rho(-1) = \rho_1$ and $\rho(1) = \rho_2$, with $\rho_2 > \rho_1 > 0$ denoting the constant densities of the two involved fluids. The viscosity function is $\eta(\varphi)$ and satisfies $\eta(-1) = \eta_1$ and $\eta(1) = \eta_2$, with η_1, η_2 denoting the viscosities of the involved fluids. For this work, they were chosen as:

$$\rho = \frac{1}{2} ((\rho_l + \rho_g) + \varphi(\rho_l - \rho_g)), \quad \eta = \frac{1}{2} ((\eta_l + \eta_g) + \varphi(\eta_l - \eta_g)). \quad (5)$$

Equations (1) and (2) are the common incompressible Navier–Stokes equations with two additional terms: The density flux $J := -b \frac{\partial \rho}{\partial \varphi} \nabla \mu$ guarantees consistency and enhances stability if the densities of the two fluids are different. The surface tension force is modelled by $\varphi \nabla \mu$. The parameter b stems from the diffuse interface approach in the Cahn–Hilliard equation Equations (3) and (4). It represents the mobility of the two-phase interface. The thickness of the diffuse interface is described by ϵ . The scaled surface tension is given by $\sigma = \frac{3}{2\sqrt{2}} \sigma^{phy}$ with the physical surface tension σ^{phy} . The function $W(\varphi)$ denotes a dimensionless potential of double-well type with two strict minima at ± 1 .

Here, we chose it as

$$W(\varphi) := \begin{cases} \frac{1}{4}(1 - \varphi^2)^2 & \text{if } |\varphi| \leq 1, \\ (|\varphi| - 1)^2 & \text{else.} \end{cases} \quad (6)$$

For different choices of W and a comparison we refer to [13].

The model (1)–(2) can be derived purely from thermodynamic principles [12]. It is postulated that the system in the whole domain can be described by the following sum of kinetic energy and Helmholtz free energy functional of Ginzburg–Landau type [14]

$$E = \frac{1}{2} \int_{\Omega} \rho |v|^2 \, dx + \sigma \int_{\Omega} \epsilon^{-1} W(\varphi) + \epsilon |\nabla \varphi|^2 \, dx. \quad (7)$$

Compared to sharp interface methods, the phase field method replaces the infinitely thin boundary between gas and liquid by a transition region with finite thickness. It describes the distribution of the different fluids by a smooth indicator function where -1 is pure gas and $+1$ is pure liquid. It follows, that all physical properties like density or viscosity vary continuously across the interface. As summarized in the review by [15], the Cahn–Hilliard–Navier–Stokes (CHNS) equations can easily handle large topological changes of the interface [16] and the interface is implicitly tracked without any prior knowledge of the position. Furthermore, one of the major advantages is that the formulation of the surface tension force in the Navier–Stokes (NS) equation conserves both the surface tension energy and kinetic energy. This can reduce spurious currents, which are purely artificial velocities around the interface, to the level of the truncation error even for low Capillary numbers [17, 18].

A. Nondimensionalization

We scale the coupled CHNS system Equations (1) to (4) with:

$$t = \frac{\hat{t}L}{U}, \quad x = L\hat{x}, \quad v = U\hat{v}, \quad p = U^2\rho_l\hat{p}, \quad \mu = \frac{U\eta_l}{L}\hat{\mu}, \quad \rho = \hat{\rho}(\rho_l + \rho_g), \quad \eta = \hat{\eta}(\eta_l + \eta_g), \quad g = \frac{U^2}{L}\hat{g}, \quad (8)$$

and apply the following nondimensional groups:

$$Re = \frac{\rho_l U L}{\eta_l}, \quad Ca = \frac{\eta_l U}{\sigma}, \quad Bo = \frac{\rho_l g L^2}{\sigma}, \quad A_\rho = \frac{\rho_l - \rho_g}{\rho_l + \rho_g}, \quad A_\eta = \frac{\eta_l - \eta_g}{\eta_l + \eta_g}, \quad Cn = \frac{\epsilon}{L}, \quad Pe_\epsilon = \frac{\epsilon L U}{b\sigma}, \quad (9)$$

where $L = \delta_{nu}$ and $U = \bar{v}_{nu}$ are the Nusselt film height and the mean film velocity, respectively. Both are calculated for a specific Reynolds number Re and the inclination angle α measured from the plate to the horizontal with:

$$\delta_{nu} = \sqrt[3]{\frac{3\eta_l^2 Re}{\rho_l^2 g \sin \alpha}}, \quad (10)$$

$$\bar{v}_{nu} = \frac{\delta_{nu}^2 \rho_l g \sin \alpha}{3\eta_l}. \quad (11)$$

In this way the physical system is characterized by the

- Reynolds number Re (inertial over viscous forces in the film),
- Capillary number Ca (viscous drag in the film over surface tension forces between film and gas),
- Bond number Bo (gravitational force in the film over surface tension forces between film and gas),
- and Atwood numbers A_ρ and A_η (density and viscosity ratios between film and gas).

The Cahn number Ca and the Peclet number Pe_ϵ stem from the Cahn–Hilliard approach and describe the dynamics of the diffuse interface.

We obtain the following nondimensionalized CHNS system[19]:

$$\rho \partial_t v + ((\rho v + J) \cdot \nabla) v - Re^{-1} \operatorname{div}(2\eta Dv) + \nabla p = -Re^{-1} \varphi \nabla \mu + Bo Ca^{-1} Re^{-1} \rho g \quad \text{in } \Omega, \quad (12)$$

$$-\operatorname{div}(v) = 0 \quad \text{in } \Omega, \quad (13)$$

$$\partial_t \varphi + v \cdot \nabla \varphi - Ca Cn Pe_\epsilon^{-1} \Delta \mu = 0 \quad \text{in } \Omega, \quad (14)$$

$$-Cn^2 \Delta \varphi + W'(\varphi) = Ca Cn \mu \quad \text{in } \Omega, \quad (15)$$

with $J := -Ca Cn Pe_\epsilon^{-1} \frac{\partial \rho}{\partial \varphi} \nabla \mu$ and

$$\rho = \frac{1}{2} (1 + \varphi A_\rho) , \quad \eta = \frac{1}{2} (1 + \varphi A_\eta) . \quad (16)$$

III. NUMERICAL METHOD

A. Discretization

For a practical implementation in a finite element scheme a time grid $0 = t_0 < t_1 < \dots < t_{m-1} < t_m < \dots < t_M = T$ on $I = [0, T]$ with non-equidistant step size $\tau^m > 0$ is introduced. Further, a triangulation \mathcal{T}_h of the domain into cells T_i is introduced such that $\mathcal{T}_h = \bigcup_{i=1}^N T_i$ covers the domain. The specific meshing is discussed in Section IV. On \mathcal{T}_h we introduced piecewise linear Lagrange finite elements $V_1 = \mathcal{P}_1$ for φ_h , μ_h and p_h and the triangular/tetrahedral Mini element $V_M = \mathcal{P}_1 \oplus \mathcal{B}_{1+d}$, denoting the space of linear polynomials enriched by a cubic bubble function, for v_h . For the derivation of the weak form as well as the proof of energy stability and thermodynamic consistency we refer to [13].

Given $\varphi^{m-1} \in V_1$, $\mu^{m-1} \in V_1$, and $v^{m-1} \in V_M$, find $\varphi_h^m \in V_1$, $\mu_h^m \in V_1$, $p_h^m \in V_1$ and $v_h^m \in V_M$, such that for all $w \in V_M$, $q \in V_1$, $\Phi \in V_1$, and $\Psi \in V_1$ the following equations hold:

$$\begin{aligned} & \frac{1}{\tau^m} \left(\frac{\rho^m + \rho^{m-1}}{2} v_h^m - \rho^{m-1} v^{m-1}, w \right) \\ & + a(\rho^{m-1} v^{m-1} + J^{m-1}, v_h^m, w) + (Re^{-1} 2\eta^{m-1} Dv_h^m, Dw) - (\text{div} w, p_h^m) \\ & + (Re^{-1} \varphi^{m-1} \nabla \mu_h^m, w) - Bo Ca^{-1} Re^{-1} (g\rho^{m-1}, w) = 0, \end{aligned} \quad (17)$$

$$-(\text{div} v_h^m, q) = 0, \quad (18)$$

$$\begin{aligned} & \frac{1}{\tau^m} (\varphi_h^m - \varphi^{m-1}, \Psi) - (\varphi^{m-1} v^{m-1}, \nabla \Psi) + \left(Re^{-1} \frac{\tau^m |\varphi^{m-1}|^2}{\rho^{m-1}} \nabla \mu_h^m, \nabla \Psi \right) \\ & + (Ca Cn Pe_\epsilon^{-1} \nabla \mu_h^m, \nabla \Psi) = 0, \end{aligned} \quad (19)$$

$$(Cn^2 \nabla \varphi_h^m, \nabla \Phi) + (W'(\varphi^{m-1}) + S_W(\varphi_h^m - \varphi^{m-1}), \Phi) - (Ca Cn \mu_h^m, \Phi) = 0, \quad (20)$$

with $J^{m-1} := -Pe_\epsilon^{-1} \frac{\partial \rho}{\partial \varphi}(\varphi^{m-1}) \nabla \mu^{m-1}$, $\rho^{m-1} := \rho(\varphi^{m-1})$, and $\eta^{m-1} := \eta(\varphi^{m-1})$. We decoupled the Navier–Stokes equation and the Cahn–Hilliard equation by using an augmented velocity field in Equation (19), see [20, 21]. In this way, one can first solve Equations (19) and (20) and thereafter Equations (17) and (18). Furthermore, for W' a stabilized linear scheme was applied, where S_W is a suitable stabilization parameter. Note that this decoupled and linearized scheme is also energy stable and thermodynamically consistent, see [13, 22].

To control the time step size we used a simple and straightforward strategy. After every time step iteration we calculated the minimal time step based on two distinct Courant numbers Co_v and Co_φ . The minimal time step τ_v^m was calculated following the well-known Courant relation, see [23]. Furthermore, to include the movement of the interface into the time step consideration, we follow [24] and replaced the velocity v^{m-1} with the phase field velocity

$$\frac{\partial_t \varphi}{|\nabla \varphi|} \approx \frac{\varphi^{m-1} - \varphi^{m-2}}{\tau^{m-1} |\nabla \varphi^{m-1}|} \quad (21)$$

to obtain τ_φ^m . The next time step τ^m was chosen as the minimum of τ_v^m and τ_φ^m as well as τ_{max} to restrict the time step size to reasonable values especially at the beginning of the simulations:

$$\tau^m = \min(\min(\tau_v^m), \min(\tau_\varphi^m), \tau_{max}) = \min \left(\min \left(\frac{Co_v h}{|v^{m-1}|} \right), \max \left(\frac{Co_\varphi \tau^{m-2} h |\nabla \varphi^{m-1}|}{|\varphi^{m-1} - \varphi^{m-2}|} \right), \tau_{max} \right) . \quad (22)$$

B. Solver

We implemented the solution scheme given in Section III A in Python3 using the finite element library FEniCS 2019.1.0 [25, 26]. For the solution of the arising linear systems and subsystems the software suite PETSc 3.8.4 [27–29] was applied. At each time step we first solved the CH system and thereafter the NS systems. The CH system was solved using the direct linear solver MUMPS 5.1.1 [30, 31]. Note that the naive usage of a Krylov method for

unsymmetric systems, e.g., GMRES, preconditioned by a simple Gauss-Seidel or successive over relaxation method to solve the CH system results in a lot of outer iterations. We refer to [32, 33] for efficient preconditioners for the CH system.

For the NS system we had to solve at every time step a linear system with the linear operator G :

$$G_{NS} = \begin{pmatrix} \frac{1}{\tau} \left(\frac{\rho^m + \rho^{m-1}}{2} v_h^m, w \right) + a(\rho^{m-1} v^{m-1} + J^{m-1}, v_h^m, w) + (Re^{-1} 2\eta^{m-1} Dv_h^m, Dw) & -(\operatorname{div} w, p_h^m) \\ & -(\operatorname{div} v_h^m, q) \\ & 0 \end{pmatrix} \quad (23)$$

$$= \begin{pmatrix} A & B^T \\ B & 0 \end{pmatrix} \quad (24)$$

Solving this large-scale saddle point system is computationally very expensive. Furthermore, large meshes forbid the usage of direct linear solvers. Therefore, we applied PETSc's GMRES method preconditioned from the right. As preconditioner an upper triangular block preconditioner for Oseen type problems was used:

$$P_{NS} = \begin{pmatrix} \hat{A} & B^T \\ 0 & -\hat{S} \end{pmatrix}, \quad (25)$$

where S is an approximation of the Schur complement given by the pressure-convection-diffusion (PCD) preconditioner

$$S^{-1} = R_p^{-1} + M_p^{-1}(I + K_p A_p^{-1}). \quad (26)$$

For details about this preconditioner we refer to [34–36]. Recently, this preconditioner was generalized to two-phase flows [37]. In this work, we used the following expressions for the matrices occurring in Equation (26):

$$M_p = \frac{Re}{\eta^{m-1}} (p_h^m, q), \quad (27)$$

$$K_p = \frac{Re}{\eta^{m-1}} a(\rho^{m-1} v^{m-1} + J^{m-1}, p_h^m, q), \quad (28)$$

$$A_p = (\nabla p, \nabla q), \quad (29)$$

$$R_p = B (\operatorname{diag}(M_v))^{-1} B^T, \quad (30)$$

$$M_v = \frac{1}{\tau} \left(\frac{\rho^m + \rho^{m-1}}{2} v_h^m, w \right) \quad (31)$$

where M_p , M_v are scaled pressure and velocity mass matrices, respectively, K_p is a scaled pressure convection matrix, and A_p is the pressure Laplacian.

For details on the implementation of the preconditioner we refer to the documentation of FENaPACK <https://fenapack.readthedocs.io>. Besides the default options in FENaPACK and PETSc the Richardson method was applied together with algebraic multigrid provided by Hypre as preconditioner for the inversion of A , R_p and A_p . For the inversion of M_p the preconditioned Chebyshev iterative method together with a Jacobi preconditioner was used.

The model and the solution scheme as well as our implementation has been extensively validated. We obtained accurate results against the well-known rising bubble benchmark by Hysing *et al.* [38], see [13]. Flows involving moving contact lines were validated against analytical solutions of spreading and pinned droplets in [39]. Again we accomplished a very good agreement. We obtained an almost perfect accordance with the analytical Nusselt film solution in [40]. For a validation involving film flows over corrugations, we matched our results with the experiments reported by [41] and the simulations by [42], see A.

IV. SIMULATION CASE AND MESH

In Figure 1 the simulation domain is illustrated. Exemplary, a triangular obstacle with base length and height of $h = 0.75$ is shown. Due to the nondimensionalization, see Section II A, h is always given relative to the film height. The geometries of the two examined microstructures are depicted in Figure 2. We chose triangular and rectangular as representative structures as they are the most simple forms with sharp corners. The solid surface was tilted to the horizontal with angle α . The flow entered the simulation domain from the left and emitted at the right. Periodic boundary conditions were applied on the left and right side of the domain. The flow was purely driven by gravity with the gravitational acceleration constant g . On the bottom wall no-slip boundary conditions were used. The size of the symmetric domain was $8L \times 4L$.

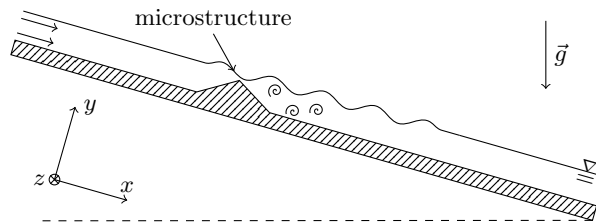


FIG. 1. Illustration of the simulation domain. Exemplary, a triangular microstructure with sharp corner is displayed.

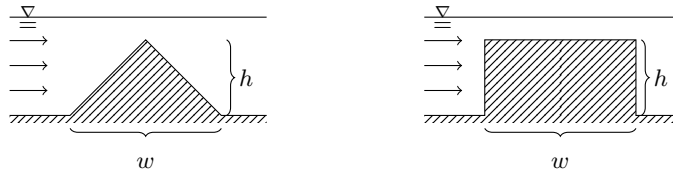


FIG. 2. Illustration of the microstructures.

Figure 3 displays the mesh used in the simulations. The two-dimensional, unstructured, triangular, periodic meshes were generated using Gmsh [43]. The background cell diameter was of size $h_{outer} = 32 Cn / 5$. The area around the interface was resolved with $h_{interface} = 4 Cn / 5$, which resulted in around five cells over the interfacial thickness. It was found by [44] that this is sufficient to accurately capture the dynamics of the interface. The film was resolved with $h_{film} = 2h_{interface}$. In this way, the mesh consisted of 1594 vertices and 3075 elements. Using the scheme from Section III A and $Cn = 0.04$ the meshing resulted in around 16,000 and 55,000 degrees of freedom for the CH and the NS system, respectively.

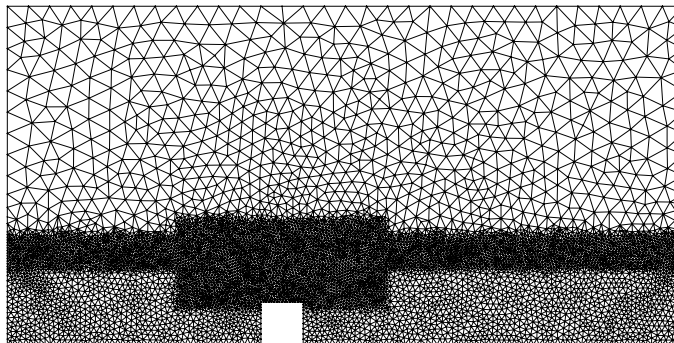


FIG. 3. Two-dimensional, unstructured, periodic, triangular mesh used in the simulations of the rectangular microstructures. It has three refinement zones: interface, film and obstacle. The size of the bounding box is $8L \times 4L$. This mesh consists of around 1594 vertices and 3075 elements.

V. FILM FLOW OVER MICROSTRUCTURES

A. Setup

To compare the stability of the liquid films, we performed simulations with Reynolds numbers Re between 10 and 70. Following [42] we assume, that two-dimensional structures can be represented with infinite depth normal to the main flow direction in a two-dimensional simulation. We initialized the simulation for a specific value of Re with a smooth film of height δ_{Nu} calculated from Equation (10). The nondimensional parameters are listed in Table I. The initial velocity of the film and the overflowing gas phase was zero, i.e., the liquid film as well as the gas phase were at rest. This corresponds to an initial inclination angle $\alpha = 0^\circ$. At the very beginning of the simulation the plate was flipped to an inclination of $\alpha = 8^\circ$. Due to the periodic domain the distance between the simulated microstructure and the subsequent microstructure was $> 7\delta$. The simulations were performed until a final time of $T = 2$ s or until a steady-state was reached.

Re	Ca	Bo	A	A_η	Cn	Pe_ϵ
10	0.04	0.0026				107
20	0.07	0.0041				169
30	0.09	0.0054				222
40	0.11	0.0066	0.99	0.99	0.04	269
50	0.13	0.0076				313
60	0.15	0.0086				353
70	0.16	0.0095				391

TABLE I. Nondimensional parameters used in the film flow simulations.

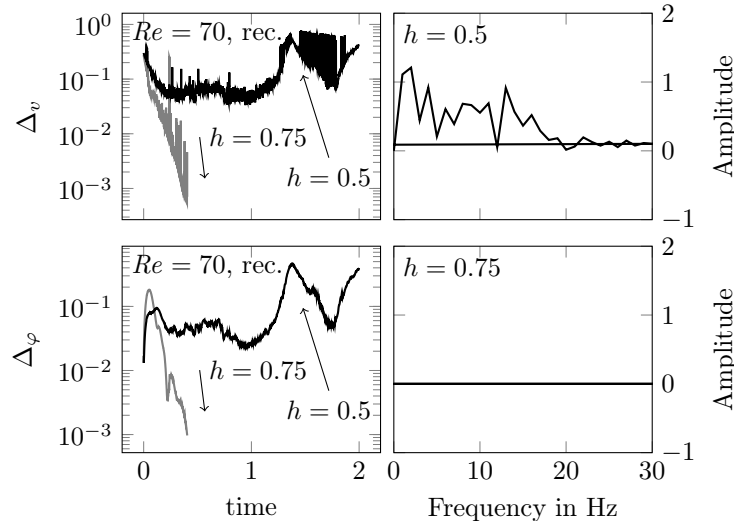


FIG. 4. Development of the steady state criteria and the corresponding amplitude spectra at $x = 3$ for 1 to 2 s.

To decide if a steady-state was reached, we looked at the change of the key variables velocity v and phase field φ over one time step [24]:

$$\Delta_v = \int_{\Omega} \frac{|v_x^m - v_x^{m-1}|}{\tau^m} dx, \quad \Delta_\varphi = \int_{\Omega} \frac{|\varphi^m - \varphi^{m-1}|}{\tau^m} dx. \quad (32)$$

Exemplarily, in Figure 4 the steady state criteria for two rectangular structures with $h = 0.75$ and $h = 0.5$ are plotted over time (left). Furthermore, we show the corresponding amplitude spectra measured at $x = 3$ for 1 to 2 s. It is clearly evident, that the large rectangular microstructure with $h = 0.75$ led to very small changes from one time step to another in the first 0.5 s (gray lines). The steady-state was reached very quickly, no waves were formed and the corresponding amplitude spectrum (bottom right panel in Figure 4) is zero. In contrast, the waves for $h = 0.5$ and $Re = 70$ completely prevented a steady-state (black lines in Figure 4).

B. Results

We observed a completely smooth film for low Re and an onset of waves for intermediate Re . For larger Re we even saw a highly distorted, almost chaotic, film with irregular waves, see below or Figure 5 and Figure 6. Qualitatively, we decided that a film is unstable if any waves were formed at all after at most 2 s. A second criteria is that the amplitude spectrum is low without any pronounced peaks. In this way, we do not take a single, stagnant bump due to retaining as a sign for an unstable film (for example, we consider the films in the fourth column from Figure 5 as stable).

In Figure 5 the film surface obtained for two microstructures (rectangular and triangular) with height and width $h = w = 0.75\delta$, $h = w = 0.5\delta$ and $h = w = 0.25\delta$ are displayed for Reynolds numbers Re ranging from 10 to 70. For comparison the film over a smooth surface is shown in the first column. The film surfaces (depicted as solid black lines) were extracted from the simulation data as the isolines where $\varphi = 0$. The microstructures are illustrated as gray insets in Figure 5. To gain more insight into the waves Figure 6 shows amplitude spectra for a choice of configurations.



FIG. 5. Shape of the liquid film interface at $\tau = 2$ s for different values of Re . The domain is compressed and cut off at a height of 2.0. All dimensions are normalized with the respective film thickness δ .

The amplitudes were calculated using a discrete Fourier transformation (DFT). The data for the DFT was extracted from the isolines, see Figure 5, at $x = 3$ (right before the microstructures) for 1 to 2 s.

The film over the smooth surface did not show any deformation for low numbers of Re . As expected, waves started to form for $Re \geq 30$, which got more and more pronounced with increasing Re . However, even for $Re = 70$, the waves stayed relatively regular. The amplitude spectra showed a pronounced, sharp peak for all Re , which is a strong sign for regular waves.

We observed, that all microstructures retained the film flow and greatly altered the film surface even for low Reynolds numbers. However, this retaining before the microstructures led to a single, large hump or ridge already observed for example by [2, 9, 45]. Compared to the film on the smooth plate, all three rectangular structures inhibited the formation of waves. This is apparent from the first row in Figure 6 where all the amplitudes are almost zero except for a sharp peak obtained for the smooth surface. The onset of the formation of waves was shifted to higher Reynolds numbers. Furthermore, we observed, that the larger the structure compared to the film thickness, the stronger the inhibition (for example compare column 1 and 3 from Figure 5). Finally, if waves were formed for a critical Re , the waves were much more irregular than in the smooth case (compare for example line 5 and 6 in column 3 from Figure 5). The dynamics of the waves can be observed in Figure 7. Here, the interfaces are displayed for the small and medium rectangular structure ($h = 0.25$ and $h = 0.5$) at six instances in time between 1.5 s and 2.0 s.

For $h = 0.25$, all films displayed very similar behavior for all Re , see the columns 2 and 5 in Figure 5. The specific effect of a small triangular compared to a small rectangular microstructure is negligible. For $Re < 30$ only a slight retaining of the film could be observed and no waves, besides from the retaining of the film, occurred. For $Re > 40$ this picture suddenly changed and very irregular waves emerged for both structures. Interestingly, the structure of the waves did not really change with even higher Re , see the second and third column in Figure 6.

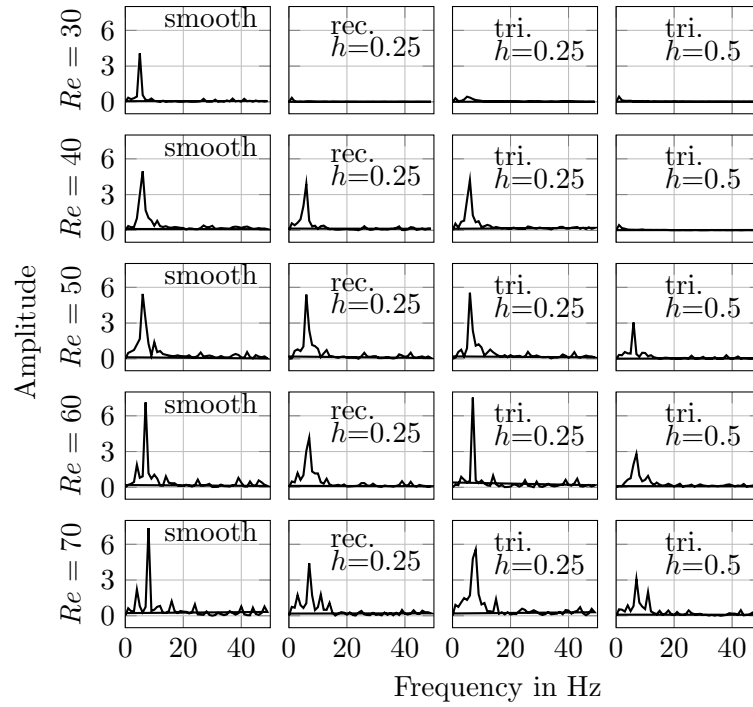


FIG. 6. Amplitude spectra for some liquid films calculated using a discrete Fourier transformation. Stable films with zero amplitude spectra are omitted. The data for the DFT was extracted from the isolines, see Figure 5, at $x = 3$ (right before the microstructures) for 1 to 2s

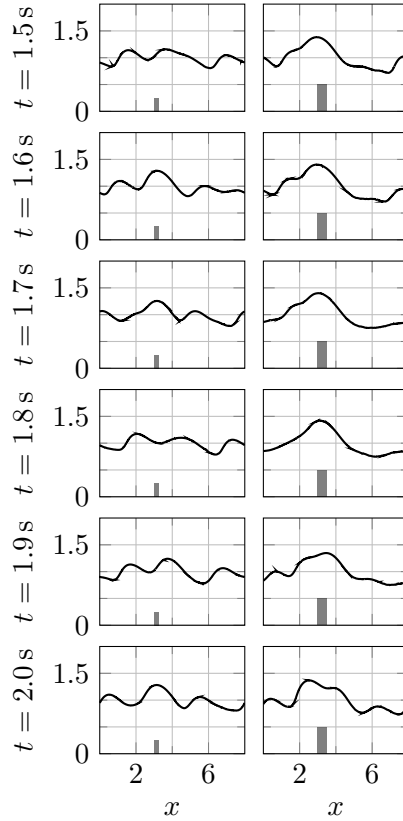


FIG. 7. Shape of the liquid film interface over rectangular microstructures at different instances of time for $Re = 70$. The domain is compressed and cut off at a height of 2.0. All dimensions are normalized with the respective film thickness δ .

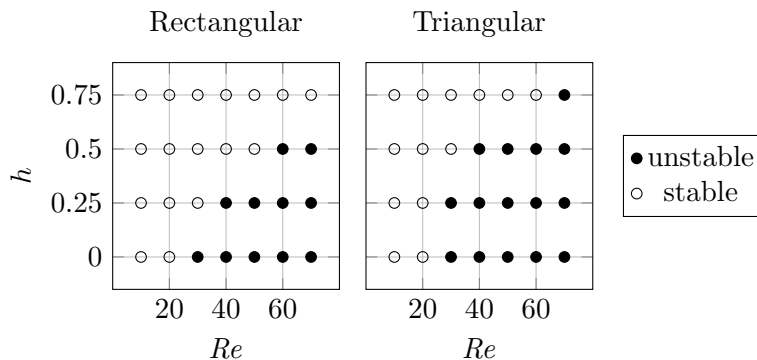


FIG. 8. Instability diagrams for the rectangular (left) and the triangular structure, each for 3 different sizes and 7 Reynolds numbers. The results obtained for the smooth plate are added at $h = 0$.

C. Discussion

The findings from Figure 5 and Figure 6 are summarized in the instability diagrams in Figure 8. Here, we plot the height of the microstructures against the Reynolds numbers. The stable films are depicted by the circular markers, whereas the unstable films are marked as filled black dots. For $h = 0$ we show the results obtained from the smooth plate in both diagrams.

We clearly observe in Figure 5, that, compared to the film on the smooth plate, all structures shift the formation of waves to higher Re . Despite being small compared to the film height, the microstructures have a relative extreme effect on the liquid film. They stabilize the film for smaller Re but greatly destabilize the film for larger Re . Furthermore, the inhibiting effect of larger structures compared to smaller structures is visible too. In general, our data indicates, that the stabilizing effect, and the inhibition of waves, of the rectangular structures is slightly larger compared to the triangular structures. Up to specific values of h and Re rectangular microstructures can prolong the formation of waves to higher Re compared to the smooth plate (see rectangular, $h = 0.5$, $Re < 50$) or even completely suppress any waves and instabilities (see rectangular, $h = 0.75$, all Re). An explanation for this stabilizing effect is the greater dissipation in films overflowing sharp corners. In case of the triangular and rectangular structure the liquid film has to overflow one two sharp corners, respectively. The dissipated energy is missing from the film to form waves. Furthermore, every structure must be bypassed by the liquid film and recirculation zones are formed before and after the structures. All these factors might be contributing to the stabilization of the liquid film by microstructures with sharp corners.

VI. CONCLUSIONS

In the presented research, we were concerned with the stability of thin liquid films overflowing single microstructures with sharp corners. The heights of the microstructures were comparable to the film thickness. The dynamics of the two-phase flow were described by the coupling between the Cahn–Hilliard and the Navier–Stokes equations. The selected solution strategy guaranteed efficient and accurate simulations. We validated our implementation against well-known experimental results.

We conducted simulations for Reynolds numbers Re between 10 and 70. The rectangular and triangular microstructures were of heights and widths of 0.25, 0.5, and 0.75 compared to the particular Nusselt film thickness. In addition, simulations over a smooth surface were performed for comparison. Our results show some very interesting stabilizing and destabilized effects. Compared to the smooth plate, all structures shift the onset of waves to higher Reynolds numbers. The specific effect of a small triangular compared to a small rectangular microstructure ($h = 0.25$) is negligible. Despite being small compared to the film height, the smaller microstructures greatly destabilized the film for higher Re . Furthermore, the larger the structure compared to the film thickness, the stronger the effect of the inhibition of the formation of waves. Finally, if waves are formed for a critical Re , the waves seem to be much more irregular than in the smooth case. In general, the inhibition of waves is stronger in the rectangular case compared to the triangular structure. In these cases the microstructures act as stabilizer for the liquid film.

Our research indicates a strong influence of the size as well as the geometrical shape of the microstructures on the stability of the liquid film. One stabilizing effect might be the dissipation of energy in the film while flowing over these sharp corners. In case of the triangular and rectangular structure the liquid film has to overflow one and two

sharp corners, respectively. It could be valuable to investigate more complex shapes perhaps with additional corners.

Appendix A: Validation against Wierschem *et al.* [41]

We validated our model and implementation by comparing our results with the experiments reported by [41]. Following the recent work by Dietze [42] as well as the review by [1] the used test case is well established. In the experiments a film of silicone oil overflowed a deep sinusoidal corrugation. The surface was inclined at 8° to the horizontal. Similar to [42] the Reynolds numbers $Re = 16.1$ and $Re = 47.95$ were simulated. Table II lists the parameters used in the simulations. Our simulation results are shown in Figure 9. They correspond to the experimental results in Wierschem *et al.* [41] Figure 3(b,d). The solid and dashed lines represent the gas-liquid interface and the stream line which separates the recirculation zone from the overflowing film. Our results are very similar to both the experimental results by Wierschem *et al.* [41] and numerical results by Dietze [42] (see Figure 14 therein). The surface shape of the films including the positions of the minimum are accurately predicted. In the corrugation through separation eddies are formed in similar sizes as in the experiment and the simulation.

Case	Re	Ca	A	Cn	Pe_ϵ	δ_{init}
A	16.1	0.063	0.99	0.04	147	0.00244
B	47.95	0.130	0.99	0.04	304	0.00297

TABLE II. Parameters used in the validation case. δ_{init} represents the initial film height taken from [42].

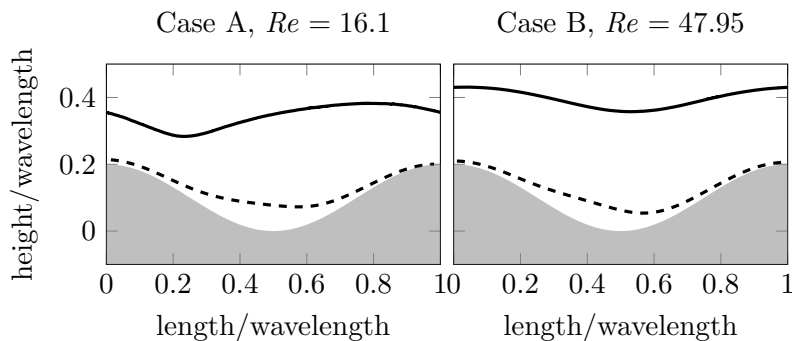


FIG. 9. Liquid film flowing over a deep sinusoidal corrugation. Corresponds to the experimental results in Wierschem *et al.* [41] Figure 3(b,d). The solid and dashed line represent the gas-liquid interface and the stream lines which separates the recirculation zone from the overflowing film.

ACKNOWLEDGMENTS

The authors acknowledge the North-German Supercomputing Alliance (HLRN) for providing HPC resources that have contributed to the research results reported in this paper and thank the German Research Foundation (DFG) for the financial support within the project RE 1705/16-1. Furthermore, we thank Christian Kahle for the fruitful discussions about the Cahn–Hilliard–Navier–Stokes equations.

-
- [1] N. Aksel and M. Schörner, *Acta Mechanica* **229**, 1453 (2018).
 - [2] M. G. Blyth and C. Pozrikidis, *Physics of Fluids* **18** (2006), 10.1063/1.2198749.
 - [3] S. Veremieiev, H. M. Thompson, and P. H. Gaskell, *Computers & Fluids* **122**, 66 (2015).
 - [4] R. V. Craster and O. K. Matar, *Reviews of Modern Physics* **81**, 1131 (2009).
 - [5] C. Brunold, J. Hunns, M. Mackley, and J. Thompson, *Chemical Engineering Science* **44**, 1227 (1989).
 - [6] M. Ozgoren, *Flow Measurement and Instrumentation* **17**, 225 (2006).
 - [7] J. C. Hu, Y. Zhou, and C. Dalton, *Experiments in Fluids* **40**, 106 (2006).
 - [8] M. M. Alam, Y. Zhou, and X. W. Wang, *Journal of Fluid Mechanics* **669**, 432 (2011).

- [9] D. Tseluiko, M. G. Blyth, and D. T. Papageorgiou, *Journal of Fluid Mechanics* **729**, 638 (2013).
- [10] P. H. Gaskell, P. K. Jimack, M. Sellier, H. M. Thompson, and M. C. T. Wilson, *Journal of Fluid Mechanics* **509**, 253 (2004).
- [11] S. Veremieiev, H. M. Thompson, Y. C. Lee, and P. H. Gaskell, *Computers and Fluids* **39**, 431 (2010).
- [12] H. Abels, H. Garcke, and G. Grün, *Mathematical Models and Methods in Applied Sciences* **22**, 1150013(40) (2012).
- [13] H. Bonart, C. Kahle, and J.-U. Repke, *Journal of Computational Physics* **399**, 108959 (2019), arXiv:1809.06689.
- [14] D. Jacqmin, *Journal of Computational Physics* **155**, 96 (1999).
- [15] M. Wörner, *Microfluidics and Nanofluidics* **12**, 841 (2012).
- [16] D. M. Anderson, G. B. McFadden, and A. A. Wheeler, *Annual Review of Fluid Mechanics* **30**, 139 (1998).
- [17] Q. He and N. Kasagi, *Fluid Dynamics Research* **40**, 497 (2008).
- [18] F. Jamshidi, H. Heibel, M. Hasert, X. Cai, O. Deutschmann, H. Marschall, and M. Wörner, *Computer Physics Communications* (2018), 10.1016/j.cpc.2018.10.015.
- [19] For better readability we omit the $\hat{\cdot}$ above all scaled variables and operators from now on. If not otherwise noted, starting from Equation (12) all variables are scaled and dimensionless.
- [20] S. Minjeaud, *Numerical Methods for Partial Differential Equations* **29**, 584 (2013).
- [21] G. Grün, F. Guillén-González, and S. Metzger, *Communications in Computational Physics* **19**, 1473 (2016).
- [22] J. Shen, X. Yang, and H. Yu, *Journal of Computational Physics* **284**, 617 (2015).
- [23] J. H. Ferziger and M. Peric, *Book* (Springer Berlin Heidelberg, Berlin, Heidelberg, 2008) p. 509, arXiv:arXiv:1011.1669v3.
- [24] S. Aland, *Journal of Computational Physics* **262**, 58 (2014), arXiv:arXiv:1307.2127v1.
- [25] M. S. Alnæs, J. Blechta, J. Hake, A. Johansson, B. Kehlet, A. Logg, C. Richardson, J. Ring, M. E. Rognes, and G. N. Wells, *Archive of Numerical Software* **3** (2015), 10.11588/ans.2015.100.20553.
- [26] A. Logg, K.-A. Mardal, and G. Wells, eds., *Automated Solution of Differential Equations by the Finite Element Method - The FEniCS Book*, Lecture Notes in Computational Science and Engineering, Vol. 84 (Springer, 2012).
- [27] S. Balay, S. Abhyankar, M. Adams, J. Brown, P. Brune, K. Buschelman, L. Dalcin, V. Eijkhout, W. Gropp, D. Kaushik, M. Knepley, D. May, L. C. McInnes, R. T. Mills, T. Munson, K. Rupp, P. Sanan, B. Smith, S. Zampini, H. Zhang, and H. Zhang, “PETSc Web page,” <http://www.mcs.anl.gov/petsc> (2018).
- [28] S. Balay, S. Abhyankar, M. Adams, J. Brown, P. Brune, K. Buschelman, L. Dalcin, V. Eijkhout, W. Gropp, D. Kaushik, M. Knepley, D. May, L. C. McInnes, R. T. Mills, T. Munson, K. Rupp, P. Sanan, B. Smith, S. Zampini, H. Zhang, and H. Zhang, *{PETS}c Users Manual*, Tech. Rep. ANL-95/11 - Revision 3.9 (Argonne National Laboratory, 2018).
- [29] S. Balay, W. D. Gropp, L. C. McInnes, and B. F. Smith, in *Modern Software Tools in Scientific Computing*, edited by E. Arge, A. M. Bruaset, and H. P. Langtangen (Birkhäuser Press, 1997) pp. 163–202.
- [30] P. R. Amestoy, I. S. Duff, J. Koster, and J.-Y. L’Excellent, *SIAM Journal on Matrix Analysis and Applications* **23**, 15 (2001).
- [31] P. R. Amestoy, A. Guermouche, J.-Y. L’Excellent, and S. Pralet, *Parallel Computing* **32**, 136 (2006).
- [32] P. Boyanova, M. Do-Quang, and M. Neytcheva, *Computational Methods in Applied Mathematics* **12**, 1 (2012).
- [33] J. Bosch, C. Kahle, and M. Stoll, *Communications in Computational Physics* **23** (2018), 10.4208/cicp.OA-2017-0037, arXiv:1610.03991.
- [34] J. Blechta, “Towards efficient numerical computation of flows of non-Newtonian fluids,” (2019).
- [35] M. A. Olshanskii and Y. V. Vassilevski, *SIAM Journal on Scientific Computing* **29**, 2686 (2007).
- [36] H. Elman, V. E. Howle, J. Shadid, R. Shuttleworth, and R. Tuminaro, *Journal of Computational Physics* **227**, 1790 (2008).
- [37] N. Bootland, A. Bentley, C. Kees, and A. Wathen, *SIAM Journal on Scientific Computing* **41**, B843 (2019), arXiv:1710.08779.
- [38] S. Hysing, S. Turek, D. Kuzmin, N. Parolini, E. Burman, S. Ganesan, and L. Tobiska, *International Journal for Numerical Methods in Fluids* **60**, 1259 (2009).
- [39] H. Bonart, J. Jung, C. Kahle, and J.-U. Repke, *Chemical Engineering & Technology* **42**, 1381 (2019).
- [40] H. Bonart and J.-U. Repke, *Chemical Engineering Transactions* **69**, 61 (2018).
- [41] A. Wierschem, T. Pollak, C. Heining, and N. Aksel, *Physics of Fluids* **22**, 113603 (2010).
- [42] G. F. Dietze, *Journal of Fluid Mechanics* **859**, 1098 (2019).
- [43] C. Geuzaine and J.-F. Remacle, *International Journal for Numerical Methods in Engineering* **79**, 1309 (2009).
- [44] X. Cai, H. Marschall, M. Wörner, and O. Deutschmann, *Chemical Engineering & Technology* **38**, 1985 (2015).
- [45] S. J. Baxter, H. Power, K. A. Cliffe, and S. Hibberd, *Physics of Fluids* **21** (2009), 10.1063/1.3082218.